Materials Horizons

ROYAL SOCIETY OF CHEMISTRY

COMMUNICATION

View Article Online
View Journal | View Issue

Cite this: *Mater. Horiz.*, 2023, **10**, 4952

Received 13th June 2023,
Accepted 1st August 2023

DOI: 10.1039/d3mh00908d

rsc.li/materials-horizons

Induction heating: an efficient methodology for the synthesis of functional core–shell nanoparticles†

Álvaro Raya-Barón, ‡[a] Sourav Ghosh, ‡[a] Jaime Mazarío, ‡[a] Víctor Varela-Izquierdo, [a] Pier-Francesco Fazzini, [a] Simon Tricard, [a] Jerome Esvan[b] and Bruno Chaudret *[a]

Induction heating has been applied for a variety of purposes over the years, including hyperthermia-induced cell death, industrial manufacturing, and heterogeneous catalysis. However, its potential in materials synthesis has not been extensively studied. Herein, we have demonstrated magnetic induction heating-assisted synthesis of core–shell nanoparticles starting from a magnetic core. The induction heating approach allows an easy synthesis of $FeNi_3$@Mo and $Fe_{2.2}C$@Mo nanoparticles containing a significantly higher amount of molybdenum on the surface than similar materials synthesized using conventional heating. Exhaustive electron microscopy, X-ray diffraction, and X-ray photoelectron spectroscopy characterization data are presented to establish the core–shell structures. Furthermore, the molybdenum shell was transformed into the Mo_2C phase, and the catalytic activity of the resulting nanoparticles tested for the propane dry reforming reaction under induction heating. Lastly, the beneficial role of induction heating-mediated synthesis was extended toward the preparation of the $FeNi_3$@WO_x core–shell nanoparticles.

New concepts

Using magnetic nanoparticles as heating agents under an alternating magnetic field is a hot research topic due to the high efficiency of heat delivery on a localized spot that these materials enable. For applications, magnetic nanoparticles may need additional functionalization; we show here that magnetic induction allows the preparation of nanoparticles displaying a magnetic core and a shell of molybdenum, a metal difficult to obtain at the zerovalent state, $FeNi_3$@Mo and $Fe_{2.2}C$@Mo. This approach yields significant benefits, depositing approximately twice as much molybdenum on the nanoparticle shell compared to a conventional thermal method in a shorter reaction time and spending lower amounts of $Mo(CO)_6$. Thus, using magnetic heating instead of thermal heating allows $FeNi_3$ or $Fe_{2.2}C$ nanoparticles to serve as both a heat source and a nucleation centre, resulting in an accurate decomposition of $Mo(CO)_6$ onto the desired spot. The resulting outer layer can be further transformed into Mo_2C under magnetic induction and used for catalytic reactions such as propane dry reforming hence demonstrating the flexibility of the approach. Finally, applying this strategy to an $FeNi_3$@W system shows that this approach may be extended to functionalize magnetic materials efficiently and accurately. Therefore, the methodology reported herein paves the way for developing innovative complex nanostructures.

[a] *LPCNO (Laboratoire de Physique et Chimie des Nano-Objets), Université de Toulouse, CNRS, INSA, UPS, 31077 Toulouse, France. E-mail: chaudret@insa-toulouse.fr*

[b] *CIRIMAT-ENSIACET, INP-ENSIACET, 4 allée Emile Monso, BP 44362, 31030 Toulouse cedex 4, France*

† Electronic supplementary information (ESI) available. See DOI: https://doi.org/10.1039/d3mh00908d

‡ Equally contributed.

Bruno Chaudret

After a long-standing relationship with the RSC, in particular as a former member of the Editorial Boards of New J Chem, Dalton Transactions and Catalysis Science & Technology as well as recipient of the Wilkinson Prize, I have been very honored to be nominated as a scientific editor of Materials Horizons. For me the journal was special since each article should bring a new concept and explain it in a separate paragraph. This requirement is largely responsible for the success of Materials Horizons over the past ten years, now a leading journal in the field of materials science.

1. Introduction

Magnetic nanoparticles (Mag-NPs) can produce high temperatures in short times and in localized spots *via* hysteresis losses when exposed to an alternating magnetic field (AMF).[1–3] They have found applications in different fields, such as catalysis,[1–3] medicine,[4] and industrial manufacturing,[5] where they offer

remarkable advantages such as improved energy efficiency, precise localized heating and swift temperature control. However, synthetic implications of the induction heating phenomena (IH) remain almost unexplored at the nanoscale.

Although the literature is teeming with examples of chain-like assemblies, nanosheets and core–shell structures assisted by static magnetic fields,[6,7] there are few instances where an AMF is used, and none that produce core–shell nanoparticles. There have been reports of metal substrates acting as a heating agent upon generating eddy currents under AMF for growing nanostructures. One example is nickel foam anchoring Ni nanoparticles on MoO_2 nanowires and NiFe-layered double hydroxides.[8] Besides, graphene and carbon nanotubes (CNTs) have been grown on metal substrates by induction heating (IH) in a chemical vapor deposition (CVD) system using Pt monocrystals,[9] Pt foils,[10] Cu foils,[11] and Ni layers[12] as the heating substrates. Cu and Cu_2O nanostructures can also be synthesized on Ni foil using IH and electrodeposition in solution.[13] Moreover, graphene, a conductive non-metal, serves as a self-heating medium for the preparation of SiC nanorods from SiO_2 NPs.[14] The possibility of using reactors filled with stainless steel balls in a coil for the synthesis of iron oxide nanoparticles[15] or CdSe[16] quantum dots (QDs) has also received attention. To the best of our knowledge, the only systems derived from the use of nanoparticles under an AMF are TiO_2-decorated Fe_3O_4,[17] and a carbon Fe_3O_4 nanocomposite.[18] However, no literature on magnetic nanoparticles acting as the substrate for the growth of metal, metal oxide or metal carbide shells is available.

On the other hand, core–shell nanoparticles are a distinct class of nanomaterials that offer unique advantages. By combining the properties of the core and shell, it is possible to tailor their physical and chemical attributes. In fact, they have found a wide range of uses in materials chemistry,[19] biomedicine,[20] and catalysis[21] due to their broad range of features. Realizing their potential in varieties of applications, numerous synthetic routes were proposed.[21,22] The most popular synthetic method for core–shell nanoparticles is the seed-mediated growth of a shell over a preformed core particle.[21,22] Inspired by this, we aimed to develop a general method for the synthesis of core–shell nanoparticles through the use of ferromagnetic nanoparticles to create metallic or metal carbide shells *via* precursor decomposition in a reducing atmosphere. Based on this, and to explore the generality of the approach, we have considered two materials for the core, *i.e.*, $FeNi_3$ and $Fe_{2.2}C$ nanoparticles, the magnetic properties of which have been studied in our group, and refractory targets which are difficult to prepare at the nanoscale, namely Mo and Mo_2C.

Interestingly, transition metal carbides have recently been proposed as substitutes for noble metals in catalysis due to their similar electronic properties.[23,24] Among them, molybdenum carbide is a promising option due to a catalytic activity similar to platinum.[25,26] In that sense, it has been employed in heterogeneous phases for a variety of processes, including synthesis gas conversion into alcohols,[27] water gas shift reaction,[28] CO_2 hydrogenation,[29] reductive biomass upgradation,[30,31] and the hydrogen evolution reaction (HER).[32] In this work, the dry reforming of propane (PDR) was selected to evaluate the catalytic activity of the Mo-based shell. PDR has gathered interest because it leads to the production of synthesis gas while valorising CO_2 ($C_3H_8 + 3CO_2 \rightleftharpoons 6CO + 4H_2$, $\Delta H^\circ = 620$ kJ mol^{-1}), and propane is regarded as a suitable hydrogen carrier due to the already existing infrastructure for its transport and storage.[33–35] Since the PDR reaction occurs at high temperatures (550 to 900 °C) and low pressures, magnetic heating assisted by commercial Fe-wool was used along with the Mag-NPs@Mo nanoparticles.[36,37]

Table 1 Abbreviation of the core–shell nanoparticles synthesized in this work

Abbreviation	Magnetic core	Metal shell	Heating mode
$FeNi_3$@Mo-TH	$FeNi_3$	Mo	Thermal
$FeNi_3$@Mo-IH	$FeNi_3$	Mo	Induction
$Fe_{2.2}C$@Mo-TH	$Fe_{2.2}C$	Mo	Thermal
$Fe_{2.2}C$@Mo-IH	$Fe_{2.2}C$	Mo	Induction
$FeNi_3$@WO_x-IH	$FeNi_3$	W	Induction

In summary, we present herein the synthesis of $FeNi_3$@Mo and $Fe_{2.2}C$@Mo nanoparticles (Mag-NP@Mo) *via* thermal and induction heating mediated decomposition of a $Mo(CO)_6$ precursor. The as-prepared samples were thoroughly characterized using transmission electron microscopy (TEM), scanning transmission electron microscopy energy-dispersive X-ray spectroscopy (STEM-EDS) elemental mapping, powder X-ray diffraction (XRD), vibrating sample magnetometry (VSM), and inductively coupled plasma atomic emission spectroscopy (ICP-AES) techniques. The differences between conventional and induction heating (IH) were investigated. Furthermore, the unprecedented functionalization of Mag-NPs with carbidic Mo, the enhancement of the Mo_2C phase by carburation, and its catalytic activity toward the PDR reaction were discussed. The results demonstrate that this approach directs the reaction towards the nanoparticle surface by utilizing the "hot spot" phenomenon. This results in the formation of refractory shells and boosts deposition yield by reducing homogeneous nucleation of molybdenum when compared to the thermal approach. Additionally, the magnetic core is preserved, resulting in high-quality core–shell nanostructures. Finally, the IH-mediated synthesis of $FeNi_3$@WO_x core–shell nanoparticles was demonstrated for scope extension purposes. The sample abbreviation is shown in Table 1.

2. Results and discussion

At first, $FeNi_3$@Mo-TH and $Fe_{2.2}C$@Mo-TH NPs were prepared by thermal decomposition of $Mo(CO)_6$ on $FeNi_3$ NPs or $Fe_{2.2}C$ NPs, respectively, at 150 °C under a 3 bar H_2 pressure, following a procedure analogous to that previously described in our group for the synthesis of $Fe_{2.2}C$@Ru,[38] namely a two-step method (see Scheme 1). First, a layer of Mo was deposited, which acted as the nucleation site for the overgrowth of a Mo shell. Each step lasted for 72 hours, and an increasing concentration of Mo was used in each step, (*i.e.*, 0.01 mmol mL^{-1} and 0.04 mmol mL^{-1}). Elemental analysis data for $FeNi_3$@Mo and $Fe_{2.2}C$@Mo NPs synthesized *via* thermal and induction heating can be found in entries 1 and 3 in Table 2. The bulk

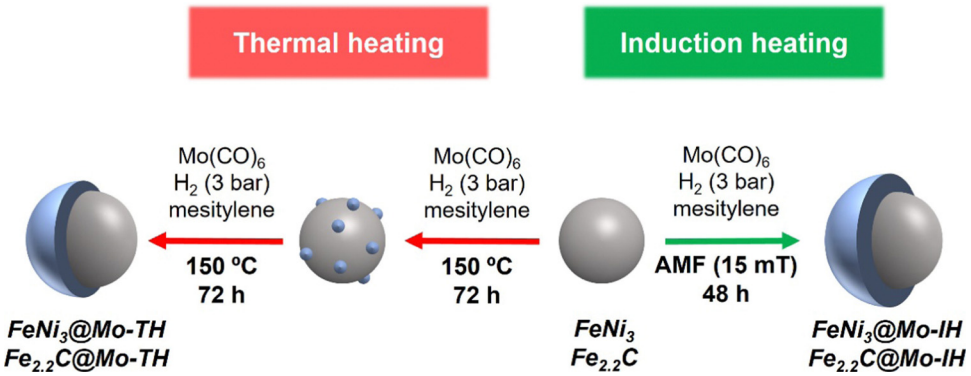

Scheme 1 Schematic representation of thermal and magnetically induced molybdenum coating on magnetic nanoparticles.

Table 2 Chemical compositions and particle sizes of $FeNi_3$@Mo and $Fe_{2.2}C$@Mo nanoparticles synthesized *via* thermal and induction heating

			ICP-AES[b] (wt%)			XPS[c] (at%)		
Entry	Material	d^a (nm)	Fe	Ni	Mo	Fe	Ni	Mo
1	$FeNi_3$@Mo-TH	14.9 ± 2.6	18	66	7	39	27	34
2	$FeNi_3$@Mo-IH	15.7 ± 2.6	18	56	14	29	16	55
3	$Fe_{2.2}C$@Mo-TH	14.8 ± 1.8	71	—	11	76	—	24
4	$Fe_{2.2}C$@Mo-IH	14.8 ± 1.8	65	—	21	51	—	49

[a] Particle size was calculated from the histogram plotted using the BF TEM images (all the histograms are shown in the ESI). [b] Mass percentage referred to the total mass of material. [c] Atomic percentage refers to the total amount of metals.

composition of $FeNi_3$@Mo-TH and $Fe_{2.2}C$@Mo-TH NPs determined by ICP-AES analysis proved the presence of Mo in the products in 7 wt% for $FeNi_3$@Mo-TH and 11 wt% for $Fe_{2.2}C$@Mo-TH (Table 2 and Table S1, ESI†).

Taking advantage of the magnetic properties of $FeNi_3$ and $Fe_{2.2}C$ precursors, Mo-coated nanoparticles were synthesized using induction heating (300 kHz, 15 mT) for 48 hours. The as-prepared $FeNi_3$@Mo-IH and $Fe_{2.2}C$@Mo-IH contained 14 wt% Mo for $FeNi_3$@Mo-IH and 21 wt% for $Fe_{2.2}C$@Mo-IH as determined by ICP-AES (Table 2 and Table S1, ESI†). Thus, the implementation of induction heating in the synthesis process enabled the achievement of greater quantities of Mo, all within a single cycle of the $Mo(CO)_6$ decomposition step, while operating under 3 bars of H_2, and using the same concentration of Mag-NPs as for thermal heating. Furthermore, the surface composition of the nanoparticles synthesized *via* thermal and induction heating was determined using the XPS technique (Table 2). Aligning with the findings observed at the bulk level, the surface analysis reveals a notable enhancement in the deposition of Mo on the bare core ($FeNi_3$ or $Fe_{2.2}C$) nanoparticles when induction heating is employed, as compared to the conventional heating method. The results from XPS data interpretation are discussed in detail in the following sections.

The morphology of the Mo-coated nanoparticles was analyzed *via* bright-field TEM (BF TEM). The particle size obtained from the histogram is tabulated in Table 2. Fig. S1 and S2 (ESI†) show the BF TEM image of parent $FeNi_3$ and $FeNi_3$@Mo-TH NPs, respectively. Both $FeNi_3$ and $FeNi_3$@Mo-TH NPs show similar polyhedral shapes. Likewise, the BF TEM image of $Fe_{2.2}C$@Mo-TH NPs showed particles that could not be distinguished from the respective parent $Fe_{2.2}C$ NPs (Fig. S3 and S4, ESI†). The particle size distribution was calculated from the histogram for the as-prepared Mag-NPs and after the Mo coating and was found to be nearly identical (Fig. S1–S4, ESI†).

Additionally, further structural characterization was carried out using the powder XRD technique. The powder XRD pattern of $FeNi_3$@Mo-TH and $Fe_{2.2}C$@Mo-TH NPs was compared with the parent $FeNi_3$ or $Fe_{2.2}C$ NPs cores (Fig. S5, ESI†). The diffraction patterns of Mo-coated NPs showed only the peaks corresponding to either $FeNi_3$ or $Fe_{2.2}C$ NPs, and no other peak that might be attributed to any Mo species (Fig. S5, ESI†). Furthermore, the presence of the Mo shell was investigated using STEM-EDX elemental mapping. STEM coupled with EDX spectroscopy confirmed the presence of molybdenum on the surface of the nanoparticles (Fig. 1 and 2). The reason why Mo

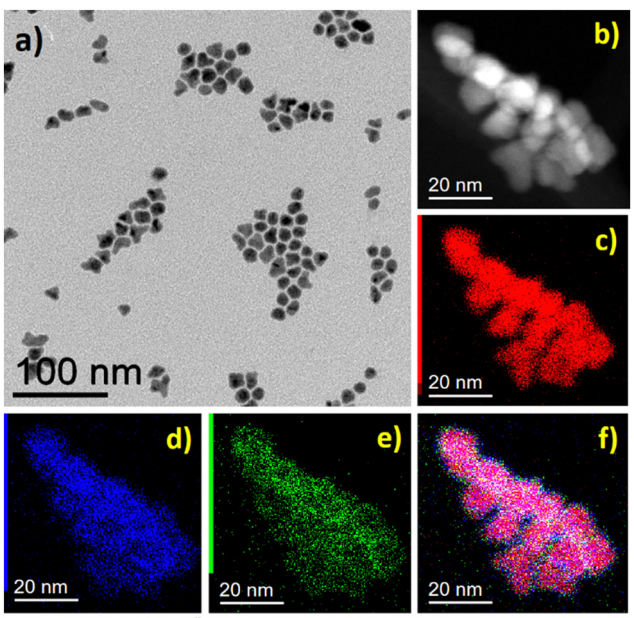

Fig. 1 $FeNi_3$@Mo-TH NPs, (a) BF TEM image, (b) STEM-HAADF image and STEM-EDX mapping of the sample, (c) Ni (red), (d) Fe (blue), (e) Mo (green), and (f) overlap of Fe, Ni, and Mo maps.

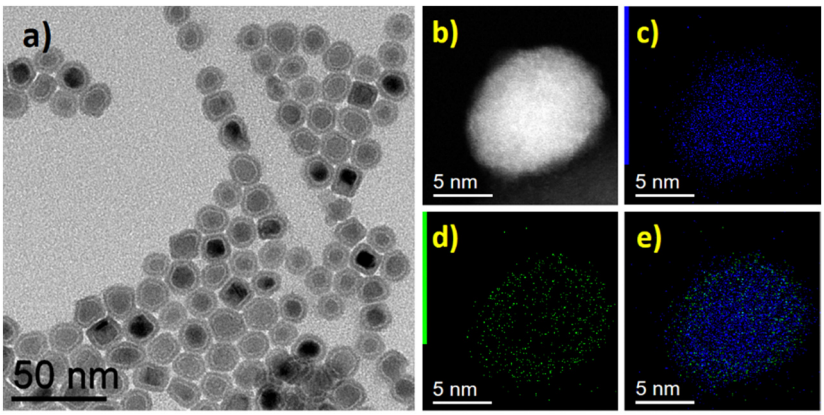

Fig. 2 $Fe_{2.2}C$@Mo-TH NPs, (a) BF TEM image, (b) STEM-HAADF image and STEM-EDX mapping showing (c) Fe (blue), (d) Mo (green), and (e) overlap of Fe and Mo maps.

was detected by ICP-AES and STEM-EDX but not by powder XRD results is probably due to the very small amount of surface molybdenum present and to its amorphous nature.

Similarly, the as-prepared $FeNi_3$@Mo-IH and $Fe_{2.2}C$@Mo-IH NPs were also characterized by BF TEM imaging, showing objects indistinguishable from their parent NPs (Fig. 3b and 4b). The $FeNi_3$@Mo-IH NPs display a mean size of 15.7 ± 2.6 nm and a polyhedral shape (Fig. S6, ESI†), while $Fe_{2.2}C$@Mo-IH NPs are spherical with a size of 14.8 ± 1.8 nm (Fig. S7, ESI†). In the same line, the powder XRD patterns matches those of the $FeNi_3$ or $Fe_{2.2}C$ cores (Fig. 3a and 4a). Despite a higher concentration of Mo present in $FeNi_3$@Mo-IH and $Fe_{2.2}C$@Mo-IH as compared to the $FeNi_3$@Mo-TH and $Fe_{2.2}C$@Mo-TH, namely a *ca.* 0.5 nm thick Mo layer, no diffraction peaks corresponding to the Mo (metallic Mo or MoO_x) species were observed. This observation can again be related to the still modest quantity of Mo present at the surface and to its amorphous nature.

Fig. 3c shows the high-resolution transmission electron microscopy (HRTEM) image of the $Fe_{2.2}C$@Mo-IH. The fast Fourier transform (FFT) analysis of the core part of the HRTEM image indicates the presence of the hexagonal $Fe_{2.2}C$ phase (Fig. 3d). In contrast, the FFT pattern of the shell was devoid of any diffraction spots. This finding emphasizes the amorphous nature of the shell. The high-resolution scanning transmission electron microscopy high-angle annular dark field (HR-STEM HAADF) image is shown in Fig. S8 (ESI†). The $Fe_{2.2}C$@Mo-IH NPs were observed to have a thin, amorphous shell measuring 1 to 2 nm, which could be attributed to Mo. To corroborate the core–shell structure, STEM-EDX mapping was conducted, and the results are shown in Fig. 3e–h. The combined Fe and Mo EDX maps confirmed that the $Fe_{2.2}C$@Mo NPs had a core–shell structure, with Mo located in the outermost layer as seen in Fig. 3h.

The HRTEM image of the $FeNi_3$@Mo-IH NPs is shown in Fig. 4c. The FFT analysis of the HRTEM image reveals a crystalline cubic $FeNi_3$ core and an amorphous Mo shell (Fig. 4d), with a thickness of 1 to 2 nm. An amorphous outer layer is also evident in the HR-STEM image (Figure S9, ESI†). The STEM-EDX

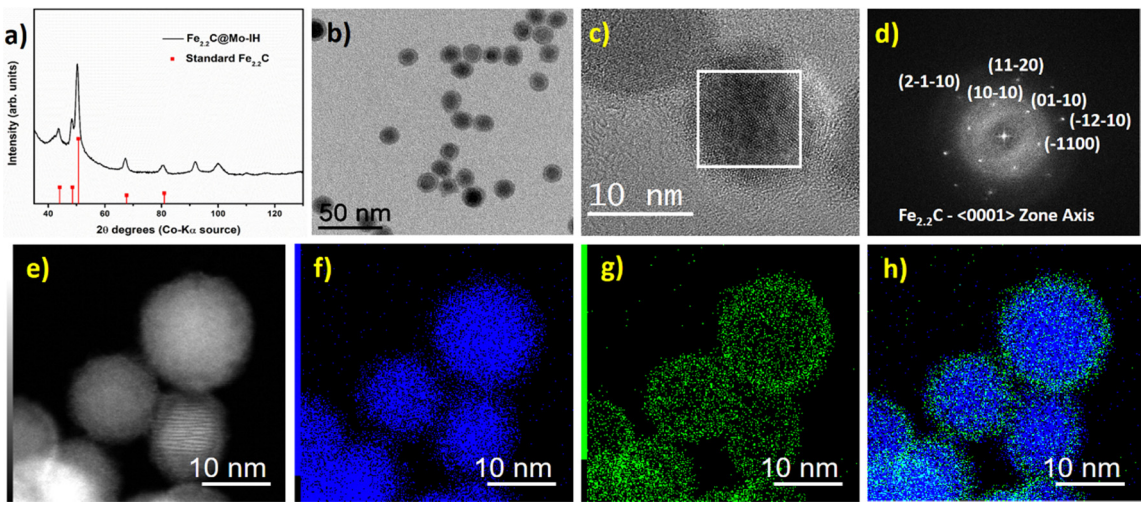

Fig. 3 $Fe_{2.2}C$@Mo-IH NPs, (a) powder XRD pattern (ICDD: 00-036-1249, red vertical drop lines for standard $Fe_{2.2}C$ pattern), (b) BF TEM micrograph, (c) HRTEM image, (d) FFT pattern derived from the white square marked zone of image c along ⟨0001⟩ zone axis, (e) STEM-HAADF image, (f)–(h) STEM-EDX elemental maps showing Fe in blue and Mo in green, and overlap of Fe and Mo maps.

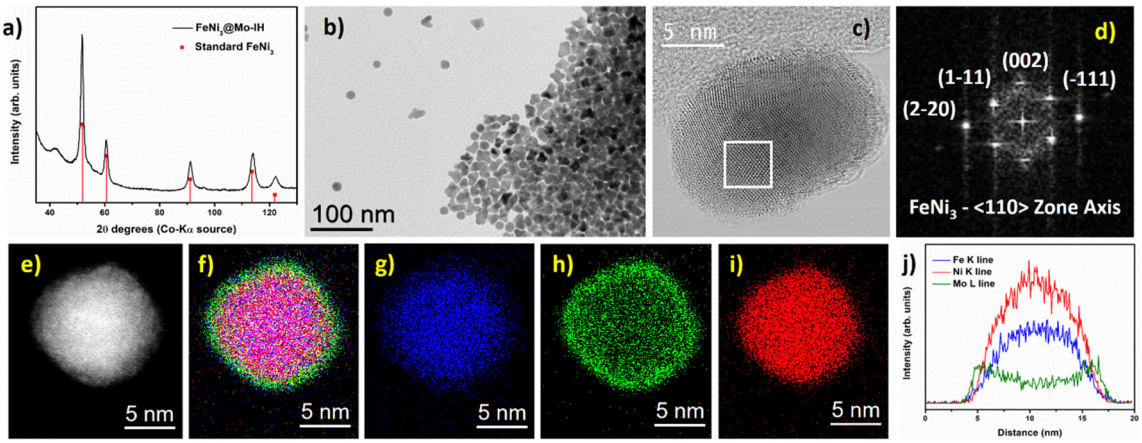

Fig. 4 $FeNi_3$@Mo-IH NPs: (a) powder XRD pattern (ICDD: 00-038-0419, red vertical drop lines for standard $FeNi_3$), (b) BF TEM micrograph, (c) HRTEM image of a single nanoparticle, (d) FFT pattern of the marked white square zone from HRTEM figure c along ⟨110⟩ zone axis, (e) STEM-HAADF image, (f)–(i) individual STEM-EDX maps showing Fe in blue, Ni in red, and Mo in green, and their overlap map, and (j) line scan profile of a single nanoparticle obtained using STEM-EDX technique (Mo L line - green, Fe K line - blue, and Ni K line – red).

elemental mapping of the $FeNi_3$@Mo-IH NPs is shown in Fig. 4e–i. The overlap of the Fe, Ni, and Mo EDX maps establishes the structure: FeNi alloy core and Mo shell. Additionally, EDX line scan analysis confirms the core–shell structure for $FeNi_3$@Mo-IH, with Mo as the outer layer (Fig. 4j).

In order to investigate the electronic state of the surface Mo layer, X-ray photoelectron spectroscopy (XPS) was performed on samples synthesized *via* thermal and induction heating. The samples were exposed to air rapidly before introduction into the spectrometer. Fig. 5 shows a tentative fitting for the Mo3d (a) and C1s (b) regions for IH samples. In the Mo3d spectrum, clear signals of oxidized Mo could be identified, with $Mo^{IV}3d_{5/2}$ appearing at 230.0 eV and $Mo^{VI}3d_{5/2}$ at 231.9 eV.[39,40] Additionally, adding components at lower binding energy (BE) makes it possible to achieve a satisfactory fit. Although this fitting (see the ESI† for a detailed procedure) may not precisely quantify Mo species, it helps identify Mo^0 (≈227.8 eV)[41,42] and carbidic Mo (≈228.4 eV).[43,44] In the case of $FeNi_3$@Mo, this carbidic peak assignment is also supported by the presence of a peak at *ca.* 282.8 eV in the C1s region.[43] Interestingly, it can be challenging to differentiate whether carbidic and Mo^0 peaks observed originate from the synthesis or from the decomposition of $Mo(CO)_6$ on surfaces under the ultra-high vacuum conditions used during analyses.[45] However, based on the low intensity of the expected CO chemisorbed peak (≈285.6 eV)[46] and the lack of precursor in the IR analyses (Fig. S12, ESI†), we can assume that the shell composed of carbidic Mo and Mo^0 originates from the IH-assisted synthesis.

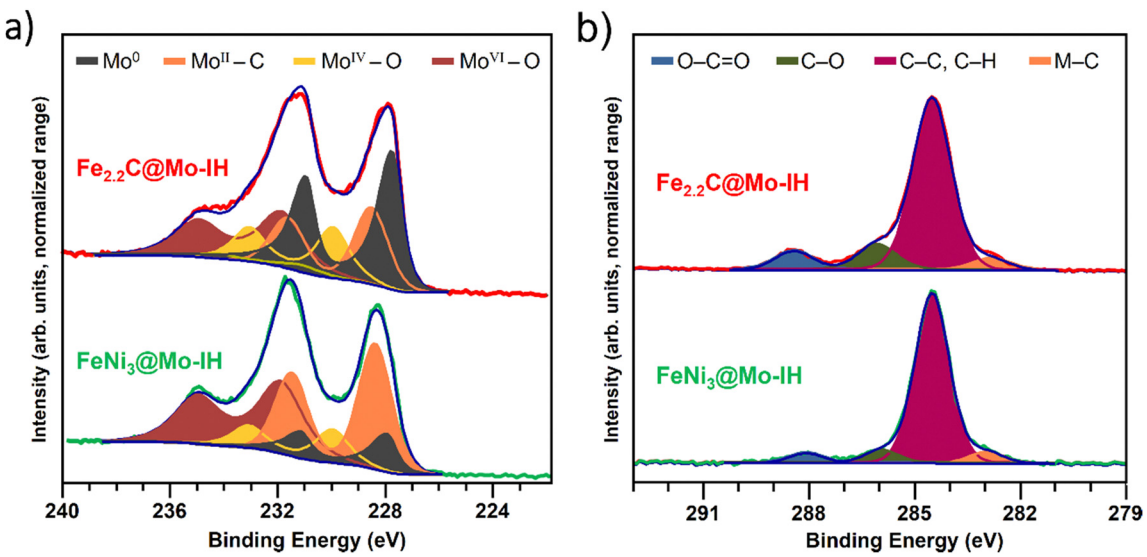

Fig. 5 (a) Mo3d and (b) C1s XPS regions for as-prepared core–shell nanoparticles assisted by induction heating after peak fitting. Note: doublet component colors are merged for a given chemical state for ease of visualization.

To investigate the reasons behind variations in Mo loading during different heating processes, we looked deeper into role of the local reaction temperature. In thermal heating, the temperature of the oil bath was considered the temperature of the solution within the Fisher–Porter bottle. In induction heating, the reaction temperature of the solution during the $Mo(CO)_6$ decomposition step was measured using an IR camera to be 165 °C (Table S3, ESI†). It is interesting to note that the $Mo(CO)_6$ boiling point is at 156 °C, and indeed a re-crystallization was observed around the neck of the Fisher–Porter bottle during the reactions in an oil bath at 150 °C. We believe it is likely that, in conventional heating, the decomposition of $Mo(CO)_6$ and the evaporation of $Mo(CO)_6$ compete, resulting in the depletion of the overall Mo concentration in the solution. On the other hand, the increased amount of Mo deposited on the magnetic cores is likely due to the generation of localized hot spots in the induction heating. This has previously been demonstrated in the case of $Fe_{2.2}C$@Ru where a surface temperature of 251 °C has been deduced from catalytic reactivity, whereas the mesitylene solution remained at 160 °C.[47] The decomposition of $Mo(CO)_6$ on the hot nanoparticles minimizes its re-crystallization on the walls of the reactor. Finally, it was observed that, the amount of Mo deposited in $FeNi_3$@Mo-IH and $Fe_{2.2}C$@Mo-IH NPs are associated with the SAR values of the bare cores $FeNi_3$ (600 W g^{-1})[48] and $Fe_{2.2}C$ (2100 W g^{-1})[49] used for the synthesis; the higher SAR values of $Fe_{2.2}C$ result in higher Mo deposition (Table S3, ESI†).

The hysteresis curves of $FeNi_3$@Mo-IH and $Fe_{2.2}C$@Mo-IH were measured using vibrating sample magnetometry (VSM) technique at 5 and 300 K (Fig. S13, ESI†). The saturation magnetization (M_s, A m^2 kg^{-1}) and coercive field (H_c, mT) values obtained at 5 and 300 K were tabulated in Table S4 (ESI†). As expected, upon deposition of the non-magnetic element (Mo), both the M_s and H_c decrease for $FeNi_3$@Mo-IH and $Fe_{2.2}C$@Mo-IH as compared to the bare core (Table S4, ESI†). The SAR measured in an AMF at a frequency of 93 kHz and 47 mT, $FeNi_3$@Mo-IH reached a value of 154 W g^{-1} and $Fe_{2.2}C$@Mo-IH one of 808 W g^{-1} (Fig. S14, ESI†). These values are substantially lower than those of their bare cores (600 W g^{-1} for $Fe_{30}Ni_{70}$ and 2100 W g^{-1} for $Fe_{2.2}C$).[48,49] Upon deposition of non-magnetic materials, the overall heating efficiency decreases for the core–shell NPs, a phenomenon previously reported.[38]

Finally, the highly loaded Mag-NP@Mo-IH NPs were chosen for induction heating mediated gas-phase propane dry reforming (PDR) reactions. The $FeNi_3$@Mo-IH and $Fe_{2.2}C$@Mo-IH NPs were further diluted in the Siralox (Siralox-5, 5% SiO_2 doped Al_2O_3) using ultrasonication (see the experimental section, ESI†). Due to the dilution of the Mag-NPs with a non-heating Siralox support, the overall heating capacity of the materials decreases. Hence, commercial Fe wool was used as an additional heating agent in order to reach the high temperatures needed for PDR (see the experimental section, ESI†). Such use of Fe wool in gas-phase catalytic reactions under induction heating has been previously demonstrated by our group.[36,37]

Before the PDR reaction, the Sirlaox samples were enriched with a Mo_2C phase by being carburized in a propane and hydrogen mixture at 670–680 °C for 90 minutes, as stated in the experimental section (ESI†). This phase is already known to enable CO_2 dissociation in dry reforming.[50] As a model system, after carburization, the $FeNi_3$@Mo_2C-IH/Siralox sample was characterized by TEM, XRD, and XPS techniques (see the ESI† for a detailed discussion). The Mo_2C phase was identified using the XRD and XPS techniques (Fig. S15–S17, ESI†). The particle size of the $FeNi_3$@Mo_2C-IH nanoparticles was slightly higher than the starting $FeNi_3$@Mo-IH NPs (Fig. S18, ESI†). The propane conversion, CO_2 conversion, carbon monoxide (CO) selectivity, and reaction temperature for different catalysts are shown in Table 3. In a control test, the pure Fe wool did not display any catalytic activity toward the PDR reaction, under the same experimental conditions. When Mo coating is followed by *in situ* carburization in the case of $FeNi_3$ and $Fe_{2.2}C$ catalysts, propane conversion increases. Remarkably, the CO selectivity for all the catalysts was found to be >92%. The TEM images of the as-prepared and the spent catalysts are shown in Fig. S21–S28 (ESI†). In all the spent catalysts, deposition of the carbon flakes and carbon filaments was observed. The β-Mo_2C phase was observed for the spent Mo-containing catalysts (Fig. S29, ESI†).

Catalytic test conditions under induction heating: 300 kHz coil, catalyst weight 150 mg, iron wool weight 100 mg, total flow of 40 mL min^{-1} (propane : CO_2 = 1 : 3; propane 10 mL min^{-1} and CO_2 30 mL min^{-1}), and WHSV = 16 000 mL g_{cat}^{-1} h^{-1}. The catalysts are carburized prior to the catalytic test. Carburization conditions: total flow of 50 mL min^{-1} (propane : H_2 = 1 : 4; propane 10 mL min^{-1} and H_2 40 mL min^{-1}) and at 670–680 °C for 90 min.

The IH technology has been proven to efficiently permit the growth of a molybdenum shell on magnetic NPs by utilizing the magnetic heating properties of precursor cores under mild reaction conditions. In this direction, the advantages of the induction heating mediated synthesis of Mag-NPs@Mo were generalized by demonstrating the synthesis of $FeNi_3$@WO_x NPs from $W(CO)_6$. In this synthesis, upon completion of the decomposition of the $W(CO)_6$ precursor in the presence of $FeNi_3$ NPs, the nanoparticles are deliberately oxidized *via* slow air diffusion (experimental section). Remarkably, the chemical stability and semiconducting properties of WO_x have found application in various fields such as electro- and photochromism, pH sensing, photo(electro)catalysis, and acid catalysis.[51–53]

The powder XRD pattern of the $FeNi_3$@WO_x-IH NPs matches the cubic $FeNi_3$ phase (Fig. 6a). Like previously, the diffraction peaks corresponding to any W (metallic W or WO_x) species were

Table 3 Propane conversion, CO selectivity, and reaction temperature (560–580 °C) are tabulated for different catalysts

Catalyst	Propane Conv. (%)	CO_2 Conv. (%)	CO Sel. (%)	T (°C)
$FeNi_3$/Siralox	73	11	97	572
$FeNi_3$@Mo-IH/Siralox	>99	19	93	570
$Fe_{2.2}C$/Siralox	2	6	94	581
$Fe_{2.2}C$@Mo-IH/Siralox	29	17	>99	584
$FeNi_3$@WO_x-IH/Siralox	60	15	92	560

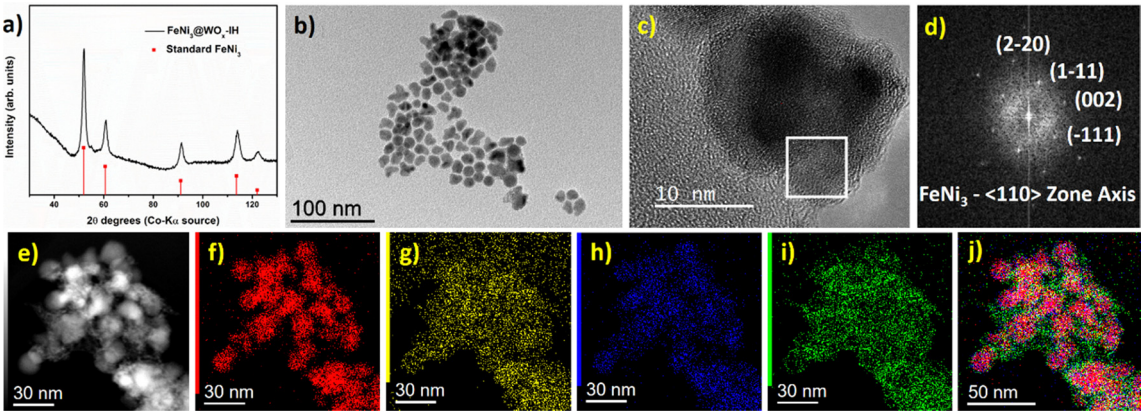

Fig. 6 $FeNi_3$@W-IH NPs, (a) powder XRD pattern (ICDD: 00-038-0419, red vertical drop lines for standard $FeNi_3$), (b) BF TEM micrograph, (c) HRTEM image and the corresponding FFT analysis (d) from the white square marked region, (e)–(j) STEM HAADF image and the respective STEM EDS elemental mapping shows Ni in red, O in yellow, Fe in blue, and W in green, and the overlap maps of W, Fe, and Ni.

not observed. The particle size and the polyhedral shapes of the $FeNi_3$@WO_x-IH NPs resemble the bare $FeNi_3$ NPs (Fig. 6b). Furthermore, through a comprehensive analysis combining HRTEM and FFT analysis, we have substantiated the presence of a cubic $FeNi_3$ core along with an amorphous WO_x shell (Fig. 6c and d). The incorporation of an amorphous WO_x layer on the $FeNi_3$ core was also observed in the STEM EDX elemental mapping (Fig. 6e–j) and was evident from the HRSTEM HAADF imaging (Fig. S30, ESI†). The Siralox diluted $FeNi_3$@WO_x-IH sample was further tested for the PDR reaction (Table 3, entry 5). The catalyst was found active for PDR reaction with ~92% CO selectivity. Hence, this specific synthesis example evidences the efficiency of the induction-heating approach and its potential to be extended to other complex materials designs.

Conclusions

This study investigated the benefits of using induction heating to create complex nanomaterials. It has been shown that the combination of magnetic induction heating with Mag-NPs, such as $Fe_{2.2}C$ and $FeNi_3$, induces $Mo(CO)_6$ decomposition and results in the synthesis of well-formed core–shell nanoparticles. These nanoparticles possess a distinctive structure wherein the outer shell contains amorphous carbidic Mo, and the magnetic phases, $FeNi_3$ or $Fe_{2.2}C$, reside in the core. By directing the decomposition towards the nanoparticle surface, this method shows notable advantages. It allows the decomposition of the precursor on the hot spots created by magnetic induction, thus resulting in the deposition of about twice the amount of molybdenum on the nanoparticle shell, in a shorter reaction time and with less $Mo(CO)_6$ precursor used than in the thermal conditions. These nanoparticles were then supported on Siralox for use in PDR and enriched with the Mo_2C phase in-situ before catalysis under a propane and hydrogen atmosphere. Finally, these new materials were shown to display interesting catalytic properties under magnetic induction.

Overall, we describe a new method for the preparation of complex nanomaterials containing a magnetic core. We have chosen for the shell a metal which is difficult to obtain at the nanoscale in a reduced form, namely molybdenum and have shown that it can be extended to an even more difficult metal, namely tungsten. This methodology can then be used for the synthesis of different complex nanostructures, depending on the desired application.

Conflicts of interest

The authors declare no conflict of interest.

Acknowledgements

The authors gratefully acknowledge the funding from the ERC Advance grant (MONACAT 2015-694159). The authors thank Alain Moreau (LCC, Toulouse) for the ICP analysis.

References

1 W. Wang, G. Tuci, C. Duong-Viet, Y. Liu, A. Rossin, L. Luconi, J.-M. Nhut, L. Nguyen-Dinh, C. Pham-Huu and G. Giambastiani, *ACS Catal.*, 2019, **9**, 7921–7935.
2 M. Estrader, K. Soulantica and B. Chaudret, *Angew. Chem., Int. Ed.*, 2022, **61**, e202207301.
3 J. Marbaix, N. Mille, J. Carrey, K. Soulantica and B. Chaudret, in *Nanoparticles in Cataysis*, ed. K. Philippot and A. Roucoux, WILEY-VCH GmbH, Germany, 1st edition, 2021, ch. 14, pp. 309–329.
4 A. Rajan and N. K. Sahu, *J. Nanopart. Res.*, 2020, **22**, 1–27.
5 O. Lucía, P. Maussion, E. J. Dede and J. M. Burdío, *IEEE Trans. Ind. Electron. Control Instrum.*, 2014, **61**, 2509–2520.
6 L. Hu, R. Zhang and Q. Chen, *Nanoscale*, 2014, **6**, 14064–14105.
7 K. Wang, Q. Yang, H. Zhang, M. Zhang, H. Jiang, C. Zheng and J. Li, *J. Mater. Chem. A*, 2023, **11**, 7802–7832.
8 G. Xiong, Y. Chen, Z. Zhou, F. Liu, X. Liu, L. Yang, Q. Liu, Y. Sang, H. Liu, X. Zhang, J. Jia and W. Zhou, *Adv. Funct. Mater.*, 2021, **31**, 2009580.
9 Y. Fu, A. V. Rudnev, G. K. H. Wiberg and M. Arenz, *Angew. Chem., Int. Ed.*, 2017, **56**, 12883–12887.

10 M. Seifert, S. Drieschner, B. M. Blaschke, L. H. Hess and J. A. Garrido, *Diamond Relat. Mater.*, 2014, **47**, 46–52.
11 R. Piner, H. Li, X. Kong, L. Tao, I. N. Kholmanov, H. Ji, W. H. Lee, J. W. Suk, J. Ye, Y. Hao, S. Chen, C. W. Magnuson, A. F. Ismach, D. Akinwande and R. S. Ruoff, *ACS Nano*, 2013, **7**, 7495–7499.
12 B. D. Sosnowchik and L. Lin, *Appl. Phys. Lett.*, 2006, **89**, 193112.
13 S. Devillers, Q. Lemineur, J. Delhalle and Z. Mekhalif, *Electrochim. Acta*, 2011, **56**, 4953–4959.
14 W. Dai, L. Lv, J. Lu, H. Hou, Q. Yan, F. E. Alam, Y. Li, X. Zeng, J. Yu, Q. Wei, X. Xu, J. Wu, N. Jiang, S. Du, R. Sun, J. Xu, C.-P. Wong and C.-T. Lin, *ACS Nano*, 2019, **13**, 1547–1554.
15 P. Sharma, N. Holliger, P. H. Pfromm, B. Liu and V. Chikan, *ACS Omega*, 2020, **5**(31), 19853–19860.
16 V. Chikan and E. J. McLaurin, *Nanomaterials*, 2016, **6**, 85.
17 C. Gómez-Polo, S. Larumbe, L. Fernández Barquín and L. Rodríguez Fernández, *J. Nanopart. Res.*, 2016, **18**, 118.
18 L. Cervera-Gabalda and C. Gómez-Polo, *Sci. Rep.*, 2023, **13**, 8913.
19 S. Wei, Q. Wang, J. Zhu, L. Sun, H. Lin and Z. Guo, *Nanoscale*, 2011, **3**, 4474–4502.
20 K. Chatterjee, S. Sarkar, K. J. Rao and S. Paria, *Adv. Colloid Interface Sci.*, 2014, **209**, 8–39.
21 M. B. Gawande, A. Goswami, T. Asefa, H. Guo, A. V. Biradar, D.-L. Peng, R. Zboril and R. S. Varma, *Chem. Soc. Rev.*, 2015, **44**, 7540–7590.
22 R. Ghosh Chaudhuri and S. Paria, *Chem. Rev.*, 2012, **112**, 2373–2433.
23 E. de Smit and B. M. Weckhuysen, *Chem. Soc. Rev.*, 2008, **37**, 2758–2781.
24 X.-H. Wang, H.-L. Hao, M.-H. Zhang, W. Li and K.-Y. Tao, *J. Solid State Chem.*, 2006, **179**, 538–543.
25 M. J. Ledoux, C. Pham Huu, J. Guille and H. Dunlop, *J. Catal.*, 1992, **134**, 383–398.
26 Y. Ma, G. Guan, X. Hao, J. Cao and A. Abudula, *Renewable Sustainable Energy Rev.*, 2017, **75**, 1101–1129.
27 S. Zaman and K. J. Smith, *Catal. Rev.: Sci. Eng.*, 2012, **54**, 41–132.
28 T. Namiki, S. Yamashita, H. Tominaga and M. Nagai, *Appl. Catal., A*, 2011, **398**, 155–160.
29 F. G. Baddour, E. J. Roberts, A. T. To, L. Wang, S. E. Habas, D. A. Ruddy, N. M. Bedford, J. Wright, C. P. Nash, J. A. Schaidle, R. L. Brutchey and N. Malmstadt, *J. Am. Chem. Soc.*, 2020, **142**, 1010–1019.
30 C. J. Chen, W. S. Lee and A. Bhan, *Appl. Catal., A*, 2016, **510**, 42–48.
31 E. F. Mai, M. A. Machado, T. E. Davies, J. A. Lopez-Sanchez and V. Teixeira da Silva, *Green Chem.*, 2014, **16**, 4092–4097.
32 J.-T. Ren, Y.-J. Song and Z.-Y. Yuan, *J. Energy Chem.*, 2019, **32**, 78–84.
33 A. Siahvashi, D. Chesterfield and A. A. Adesina, *Chem. Eng. Sci.*, 2013, **93**, 313–325.
34 Z. O. Malaibari, E. Croiset, A. Amin and W. Epling, *Appl. Catal., A*, 2015, **490**, 80–92.
35 A. Siahvashi and A. A. Adesina, *Int. J. Hydrogen Energy*, 2018, **43**, 17195–17204.
36 S. Ghosh, T. Ourlin, P. –F. Fazzini, L.-M. Lacroix, S. Tricard, J. Esvan, S. Cayez and B. Chaudret, *ChemSusChem*, 2023, **16**, e202201724.
37 S. Ghosh, S. Gupta, M. Gregoire, T. Ourlin, P.-F. Fazzini, E. Abi-Aad, C. Poupin and B. Chaudret, *Nanomaterials*, 2023, **13**(9), 1474.
38 J. M. Asensio, A. B. Miguel, P.-F. Fazzini, P. W. N. M. van Leeuwen and B. Chaudret, *Angew. Chem., Int. Ed.*, 2019, **58**, 11306–11310.
39 J.-G. Choi and L. T. Thompson, *Appl. Surf. Sci.*, 1996, **93**, 143–149.
40 J. Baltrusaitis, B. Mendoza-Sanchez, V. Fernandez, R. Veenstra, N. Dukstiene, A. Roberts and N. Fairley, *Appl. Surf. Sci.*, 2015, **326**, 151–161.
41 M. Watschinger, K. Ploner, D. Winkler, J. Kunze-Liebhäuser, B. Klötzer and S. Penner, *Rev. Sci. Instrum.*, 2021, **92**(2), 024105.
42 C. J. Powell, *J. Electron Spectrosc. Relat. Phenom.*, 2012, **185**, 1–3.
43 K. Oshikawa, M. Nagai and S. Omi, *J. Phys. Chem. B*, 2001, **105**, 9124–9131.
44 J. Gao, Y. Wu, C. Jia, Z. Zhong, F. Gao, Y. Yang and B. Liu, *Catal. Commun.*, 2016, **84**, 147–150.
45 C.-C. Cho and S. L. Bernasek, *J. Vac. Sci. Technol., A*, 1987, **5**, 1088–1090.
46 F. Zaera, *J. Phys. Chem.*, 1992, **96**, 4609–4615.
47 Z. J. Díaz-Puerto, Á. Raya-Barón, P. W. N. M. van Leeuwen, J. M. Asensio and B. Chaudret, *Nanoscale*, 2021, **13**, 12438–12442.
48 D. De Masi, J. M. Asensio, P.-F. Fazzini, L.-M. Lacroix and B. Chaudret, *Angew. Chem., Int. Ed.*, 2020, **59**, 6187–6191.
49 A. Bordet, L.-M. Lacroix, P.-F. Fazzini, J. Carrey, K. Soulantica and B. Chaudret, *Angew. Chem., Int. Ed.*, 2016, **55**, 15894–15898.
50 Y. Diao, X. Zhang, Y. Liu, B. Chen, G. Wu and C. Shi, *Appl. Catal., B*, 2022, **301**, 120779.
51 C. C. Mardare and A. W. Hassel, *Phys. Status Solidi*, 2019, **216**, 1900047.
52 T. H. Wondimu, A. W. Bayeh, D. M. Kabtamu, Q. Xu, P. Leung and A. A. Shah, *Int. J. Hydrogen Energy*, 2022, **47**, 20378–20397.
53 H. Hattori and Y. Ono. *Solid acid catalysis: from fundamentals to applications*. CRC Press, 2015.